



Efficient reduced-order thermal modelling of scanning laser melting for additive manufacturing

Guangyu Chen^{*}, Jialuo Ding, Yongle Sun, Xin Chen, Chong Wang, Goncalo Rodrigues Pardal, Stewart Williams

Welding and Additive Manufacturing Centre, Cranfield University, Cranfield MK43 0AL, UK

ARTICLE INFO

Associate Editor: Jingjing Li

Keywords:

Scanning laser
Dynamic convection boundary
Finite element method
Additive manufacturing
Welding

ABSTRACT

Additive manufacturing (AM) with a scanning laser (SL) to independently control melt pool shape has the potential to achieve part building with high geometric accuracy and complexity. An innovative dynamic convection boundary (DCB) method is proposed to develop a reduced-order finite element (FE) model to accelerate the thermal analysis of a SL process for AM. The DCB method approximates the thermal conduction of the adjacent material around the bead region by using a convection boundary condition that can be dynamically adjusted during the numerical solution. Thereby, a smaller problem domain and fewer elements are involved in the reduced-order FE modelling. A non-oscillating equivalent bar-shaped heat source was also introduced as a simplified substitution for a high oscillation frequency SL heat source. The DCB-based reduced-order thermal model achieved over 99 % accuracy compared to the full-scale model but reduced the element amount by 73 % and the computational time by 58 %. The use of the bar-shaped equivalent heat source can further enhance computational efficiency without compromising the prediction accuracy of a high oscillation frequency SL process. The DCB-based reduced-order thermal modelling method and equivalent heat source could be adopted to boost extensive parametric analysis and optimisation for novel AM processes. Study on large structures AM could also be facilitated by simplifying the computation at critical regions. This study can also enable efficient thermal analyses of different manufacturing processes, such as welding, cladding, and marking.

1. Introduction

Additive manufacturing (AM) has become an increasingly adopted net/near-net shaping technology that boosts the industrial applications of rapid prototyping and sustainable manufacturing. AM offers many unrivalled benefits, such as low material waste, short lead time, and high design flexibility, as compared to conventional subtractive manufacturing (Herzog et al., 2016). In recent AM process innovation, the potential of using a scanning laser (SL) in metal AM has been revealed and investigated. Gong et al. (2020) introduced a novel AM approach integrating a SL and a cold metal transfer (CMT) arc to balance the surface accuracy, deposition efficiency, and mechanical properties of the deposited parts. G. Chen et al. (2022) introduced a multi-energy source (MES) method employing a SL to achieve independent control of layer width and height in a wire-based directed energy deposition (w-DED) AM process, in which a high-power SL was integrated to reshape the melt pool and control the bead shape, thereby enabling the

bead width to be independently controlled by the SL. Chen et al.'s work has demonstrated the great potential of SL to be applied in the AM process for improving bead shape control and geometry printing accuracy. However, limited research has focused on the thermal characteristics of the SL-assisted AM processes. The thermal condition plays a key role in determining the metallurgical and mechanical response of the material, and hence understanding the distinct temperature distribution and evolution is essential for further developing the SL-assisted AM.

The finite element (FE) method is one of the most effective techniques for thermal analysis. In recent decades, FE has been widely used for studying the thermal behaviour in AM processes. X. Chen et al. (2022) developed a three-dimensional wire-feeding FE model to study wire-based plasma arc additive manufacturing. Li and Gu (2014) studied the thermal behaviour during the selective laser melting (SLM) of commercially pure titanium powder using a three-dimensional FE model. Ding et al. (2011) investigated the stress evolution during the thermal cycles of the wire-arc AM process with the help of a

^{*} Corresponding author.

E-mail address: guangyu.chen@cranfield.ac.uk (G. Chen).

<https://doi.org/10.1016/j.jmatprotec.2023.118163>

Received 2 July 2023; Received in revised form 7 September 2023; Accepted 22 September 2023

Available online 23 September 2023

0924-0136/© 2023 The Author(s). Published by Elsevier B.V. This is an open access article under the CC BY license (<http://creativecommons.org/licenses/by/4.0/>).

thermomechanical FE model. Loh et al. (2015) created an FE model on SLM that considers powder-to-solid transition together with an effective method to achieve volume shrinkage and material removal. Wang et al. (2022) developed a three-dimensional steady-state FE model with two independent circular surface heat sources to analyse the thermal behaviour in hybrid PTA-laser AM of Ti-6Al-4V. However, FE modellings of AM processes are recognised to be rather time-consuming, especially when simulating dynamic processes such as the SL-assisted AM for large components, which require small time increments and lots of elements (Ding et al., 2011). The graded meshing strategy, which uses larger elements in regions farther away from the heat source, is commonly used to reduce the number of elements (Huang and Usmani, 1994). However, it is difficult to mesh complex structures with graded brick elements. Instead, pyramid or wedge elements are usually used, which have a negative effect on computational efficiency and convergence (Ruppert, 1995). The self-adaptive mesh refinement technique developed in the 1970s (De et al., 1983) has been also used in some FE modellings (Joshi et al., 2004). This method allows the mesh grid to be regenerated during the modelling to adapt to the evolving solution, thereby reducing the number of elements. The limitation of the self-adaptive mesh refinement technique is that it involves a frequent regeneration of the mesh grid after each solution increment, which increases the computational time of the modelling. Despite the significantly reduced element number, the mesh refinement itself can be computationally demanding and time-consuming. Many studies were conducted to improve the computational efficiency of mesh grid regeneration. Huang and Murakawa (2016) developed a dynamic mesh refining method (DMRM) with multi-level refinement for the thermal-mechanical analysis of line heating with a moving heat source that allowed regeneration of the mesh grid in a larger specified time interval rather than each time increment. Huang et al. (2019) proposed a computation scheme based on heat transfer localization and dual meshes for the thermal analysis of large-scale welded structures. The computation accuracy is guaranteed by a local fine mesh model with size determined by a theoretical solution and a global coarse mesh model with equivalent heat input. These studies have boosted the efficiency of grid regeneration. However, a certain amount of computational time was still required.

From the view of simplifying the governing equations, Ding et al. (2011) introduced a steady-state approach to overcome the long computational time during the modelling of wire arc additive manufacturing (WAAM). In their approach, instead of using a time increment scheme to model the moving heat source, the steady state of the AM process associated with an Eulerian reference frame was simulated, in which the heat source was kept stationary while the material "flowed" through the mesh. Such a treatment converted a transient problem in the Lagrangian configuration to a steady-state problem in the Eulerian configuration, thereby markedly simplifying the governing equations and numerical solution. However, the Eulerian steady-state approach can only be utilised for quasi-steady-state AM processes, such as a single-direction WAAM process on a long plate. It is unsuitable for a highly dynamic process like the SL-assisted AM, since for SL the moving direction of the laser beam is not constant, but rather keeps altering during the scanning.

Another challenge for an efficient thermal model of the SL-assisted AM process is the representation of the heat source. Previous studies on SL modellings mainly adopted a Gaussian heat source model in the transient thermal analysis. Chen and Lee (1983) calculated the temperature profiles of a semi-infinite slab heated with a scanning laser beam using a Gaussian heat source. Cline and Anthony (1977) derived a thermal analysis for laser heating and melting materials for a Gaussian source moving at a constant velocity. Mirazimzadeh et al. (2022) investigate the thermo-mechanical characteristics of different scanning patterns for laser cladding-based additive manufacturing processes with a Gaussian-distributed heat source. In some studies, a concept of averaging Gaussian distribution along the crosswise scanning direction was

introduced to represent the SL heat source and simplify the modelling. Cline (1983) used a line heat source to represent SL in a 2D thermal model for studying the steady state of the temperature distribution on the substrate. In Basak et al. (2016), the spatial profile of a Gaussian moving heat source was also averaged crosswise, fitted with a 10th-degree polynomial, and then used as a line heat source applied to the thermal model. However, the accuracy of using these simplified line heat sources to replace the SL moving heat source has yet to be verified. If the multi-direction transient SL heat source can be replaced by an equivalent single-direction moving heat source, then the crosswise scanning transients could be neglected without loss of model accuracy. Moreover, the Eulerian steady-state approach could be also applied to the SL numerical modelling for long components, which has significant implications for efficient FE modelling.

From the above review of the literature, it is concluded that more effective ways to improve the computational efficiency of the SL-assisted AM modellings still need to be developed. In this study, an efficient reduced-order thermal model based on an innovative dynamic convection boundary (DCB) method is introduced to improve the computational efficiency of the SL modelling. The DCB method replaces the thermal conduction of a major part of the substrate with a new type of solution-dependent self-adjusting convection at the interface boundary. Thereby, the majority of the substrate can be removed and only the region of major interest is considered. The DCB method was applied to the efficient modelling of a SL process to demonstrate the dynamic thermal characteristics with different laser oscillation frequencies. SL experiments were also conducted for model calibration and validation. The results of the DCB-based reduced-order thermal model agree well with the experimental measurements and the full-scale thermal model results. In addition, a bar-shaped equivalent heat source was introduced as a simplified substitution of the SL heat source with high oscillation frequencies, which can be used to further enhance the modelling efficiency. The efficient DCB-based reduced-order thermal modelling method and equivalent heat source could be adopted to enable extensive parametric sensitivity analysis for the AM process optimisation. The high computational efficiency of these two methods can tremendously boost optimisation solution that involves repeating computations. Thermal analysis on large structure AM could also be facilitated by simplifying computation at critical regions. Apart from the AM process, this study could be also applied to the modelling of other SL processes such as welding (Rubben et al., 1997), cladding (Cui et al., 2007), and marking (Noor et al., 1994).

2. Methodology

2.1. Experiment

2.1.1. Material and equipment

SL experiments were designed to provide temperature history data for the calibration and validation of the thermal FE models. Fig. 1a schematically shows the experimental setup for the SL melting process. S275 mild steel plates with dimensions of 200 mm × 200 mm × 25 mm were used as substrates. A JK 3000FL 3 kW continuous-wave fibre laser with a wavelength of 1.08 μm was used as the heat source, which oscillated crosswise (Fig. 1b). The laser beam was redirected by a Ray-lase Superscan-III galvanometer-based scanner (GS) head and projected vertically onto the substrate without material addition. The focus distance of the GS was 620 mm, and the minimum focused laser beam size was 0.3 mm. During the SL experiment, the laser beam was defocused by moving the substrate closer to the GS, and a laser beam size of 4 mm was used. The laser power was measured by a Laserpoint W-12 K-D55-SHC-U laser calorimeter.

A FLIR A325 thermal camera was used with a FOL18 IR lens to capture the thermal images of the substrate and melt pool during the SL process. The surface of the substrate was cleaned with acetone and coated with graphite spray, which increased and homogenized the

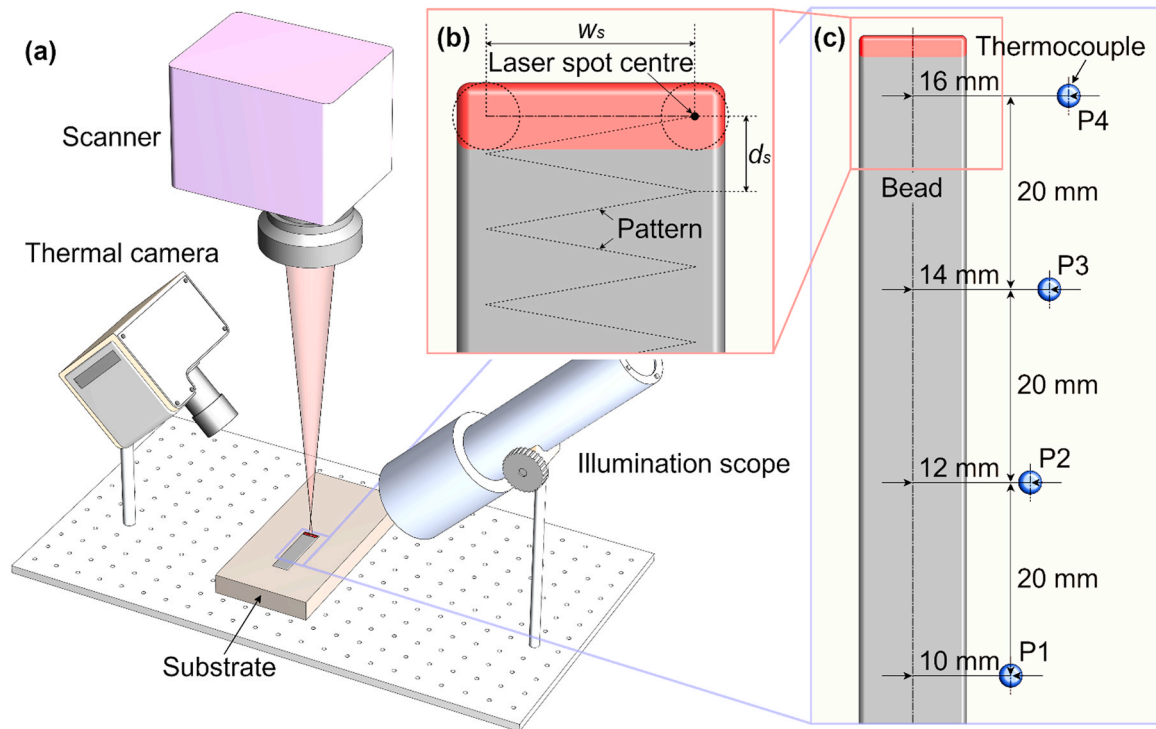


Fig. 1. (a) Configuration of the SL experiment, (b) laser scanning pattern, and (c) positions of the thermocouples.

absorptivity of the surface for the given laser energy. The graphite coating can also reduce the reflection of the substrate surface, improving the capture of thermal images and resulting in better temperature measurement accuracy and higher imaging quality (Kim and Feng,

2016). Four K-Type thermocouples were attached to the substrate surface (Fig. 1c) to measure the temperature histories at four positions with different distances to the centre of the bead. The photos of the experimental equipment, substrate, and thermocouples arrangement are

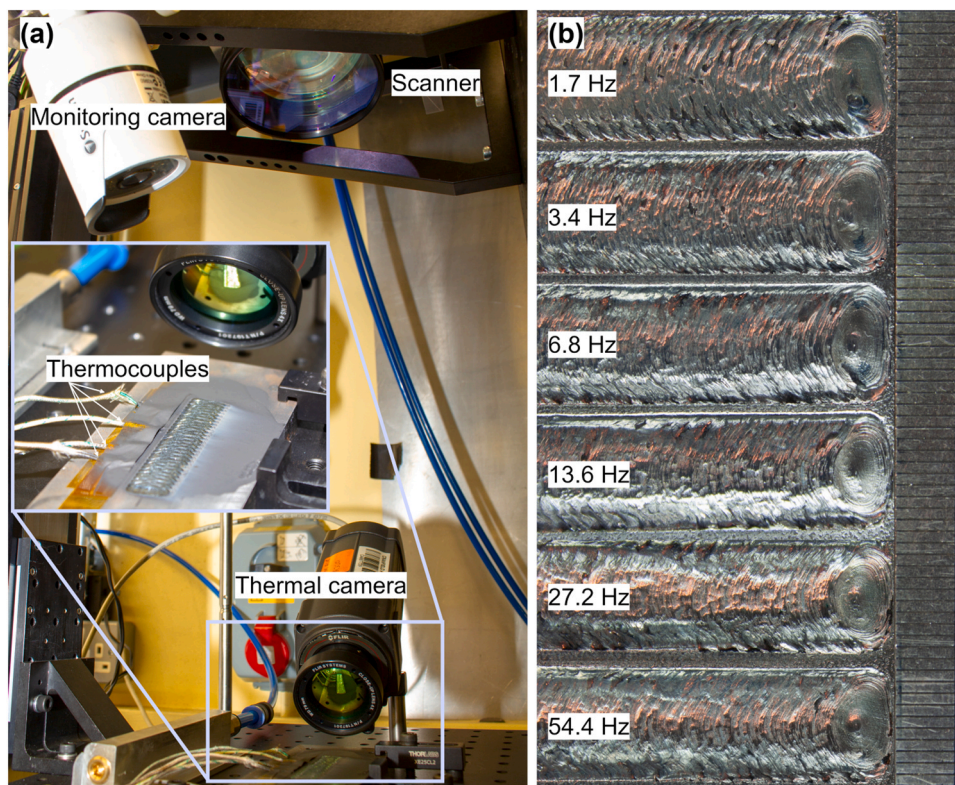


Fig. 2. (a) Photos of the experimental equipment, substrate, and thermocouples arrangement, and (b) substrate geometries of the SL processes with different oscillation frequencies.

shown in Fig. 2a.

2.1.2. Methods

The scanning pattern of the GS was defined and controlled by the SCAPS SAMLIGHT scanner application software installed in a controlling personal computer (PC). A saw-wave oscillation pattern was applied, as illustrated in Fig. 1b.

The scanning width (w_s) was defined by the crosswise moving distance of the laser beam centre and was set to be 10 mm. The oscillation frequency (F_s) was determined by the scanning speed (v_s) and the scanning width (w_s) of the SL, see Eq. (1). The increment of the scanning pattern (d_s) is determined by the oscillation frequency (F_s) and the advancing speed (v_a), see Eq. (2):

$$F_s = \frac{v_s}{2w_s} \quad (1)$$

$$d_s = \frac{v_a}{F_s} \quad (2)$$

The F_s ranged from 1.7 to 54.4 Hz, and correspondingly d_s ranged from 2 to 0.0625 mm with v_a being 3.4 mm/s. The substrate geometries of the SL processes with different oscillation frequencies are shown in Fig. 2b.

For thermal imaging, five different oscillation frequencies were considered, as shown in Table 1. A higher laser power of 2.7 kW was adopted to provide sufficient energy for a suitable melt pool size to facilitate thermal imaging. When measuring the temperature history using the thermocouples, a lower laser power of 1.45 kW was used to avoid damage to the thermocouples, and meanwhile, a lower oscillation frequency of 1.7 Hz was used to allow a longer response time for the thermocouples to capture the fluctuation of the temperature.

2.2. Finite element modelling

2.2.1. Dynamic convection boundary (DCB) method

In thermodynamics, convection is the heat transfer due to the bulk motion of a fluid medium (air, water etc.), whereas thermal conduction represents the heat transfer within a solid material (Incropera et al., 2007). The convection and the thermal conduction in the FE modelling are expressed using the following Eqs. (3) and (4), respectively:

$$Q_{cv} = hA(T_b - T_m)t \quad (3)$$

$$Q_{cd} = \frac{\lambda}{L}A(T_1 - T_2)t \quad (4)$$

where Q_{cv} represents the energy that transfers through the convection boundary, h is the convection coefficient determined by the type and condition of the heat transfer medium, A is the area of the boundary, T_b is the nodal temperature at the boundary as part of the nodal result, T_m is the bulk temperature of the heat transfer medium, and t is the time. Q_{cd} represents the energy that is transferred by thermal conduction, λ is the thermal conductivity of the material, L is the length of the concerned element along the conduction direction, T_1 and T_2 are the temperatures of the computed node and its adjacent node. We can see that the equations for thermal conduction and convection are similar in mathe-

matical form.

The concept of the DCB is introduced to replace the thermal conduction of the adjacent material with a convection interface, on which a new boundary condition is applied. In this way, a significant amount of material can be removed, and a reduced-order thermal model can be developed. The idea that part of the problem domain is omitted and a new boundary condition is imposed on the target region for compensation has been explored in arc welding modelling (Shin and Boo, 2022), but no such attempt has been reported for AM modelling.

The challenge for the aforementioned idea is that thermal conduction and convection are not entirely the same in the calculation of heat flux. Fig. 3a and b illustrate the difference between thermal conduction and convection in the FE modelling. In the thermal conduction modelling as indicated in Fig. 3a, the temperature of the adjacent node, T_2 , is part of the FE model solution and keeps changing over time. In the convection modelling as indicated in Fig. 3b, the heat transfer medium temperature, T_m , is normally set as a constant in the pre-processing stage. When heated by the energy source, the increased T_2 would slow down the thermal conduction, whereas the convection would not be affected due to the constant T_m . Therefore, when replacing the adjacent material with a convection interface, T_m needs to be adjusted during the FE modelling to take into account the evolution of the T_2 .

To dynamically adjust the T_m and approximate the thermal conduction, a solution-dependent iteration function was introduced in the DCB method to recalculate T_m after each solution increment. Fig. 4a illustrates the principle of the DCB method. In the DCB method, T_m can be adjusted during the SL modelling to approximate the temperature change of the adjacent material which is replaced with a convection interface. Eq. (5) estimates the thermal energy of the adjacent material:

$$Q_{ad(i)} = Q_{input} + (1 - a_{output})^{dt} Q_{ad(i-1)} \quad (5)$$

where $Q_{ad(i)}$ and $Q_{ad(i-1)}$ represent the thermal energy of the adjacent material at the current time step and previous time step, respectively; Q_{input} represents the energy transferred from the bead region to the adjacent material; dt is the time increment, and a_{output} is an energy output coefficient that is set to control how fast the thermal energy of the adjacent material decreases as an exponential function of time increment. Moreover, Eqs. (6) and (7) are used to calculate $Q_{ad(i)}$ and Q_{input} :

$$Q_{ad(i)} = T_{m(i)} C \rho \quad (6)$$

$$Q_{input} = a_{input} dt (T_{interface} - T_{m(i-1)}) C \rho \quad (7)$$

where C is the specific heat capacity and ρ is the density; $T_{m(i)}$ and $T_{m(i-1)}$ represent the temperatures of the adjacent material at the current time step and the previous time step, respectively; $T_{interface}$ is the temperature of the DCB interface at the previous time step; a_{input} is introduced as an energy input coefficient to determine how much additional thermal energy is transferred from the bead region to the adjacent material per unit of time based on the thermal gradient. Compared to the thermal gradient at the interface, the specific heat capacity and density only change slightly with temperature and hence they are set as constant for simplicity. Thereby, a solution-dependent iteration function for the T_m in the DCB is proposed by combining Eqs. (5)–(7):

$$T_{m(i)} = a_{input} dt (T_{interface} - T_{m(i-1)}) + (1 - a_{output})^{dt} T_{m(i-1)} \quad (8)$$

It should be noted that the above iteration function works as an empirical model to approximate the change of the adjacent material temperature during the heat conduction, and hence a calibration of the DCB method is needed. A flow chart that explains the DCB subroutine during the FE modelling is shown in Fig. 4b.

2.2.2. Heat source models

A surface Gaussian heat source model was used to represent the laser beam power distribution profile in the SL process (PAVELIC et al.,

Table 1
Parameters for the SL experiment.

Power/(kW)	Oscillation frequency/(Hz)
1.45	1.7
2.7	1.7
2.7	3.4
2.7	6.8
2.7	13.6
2.7	27.2
2.7	54.4

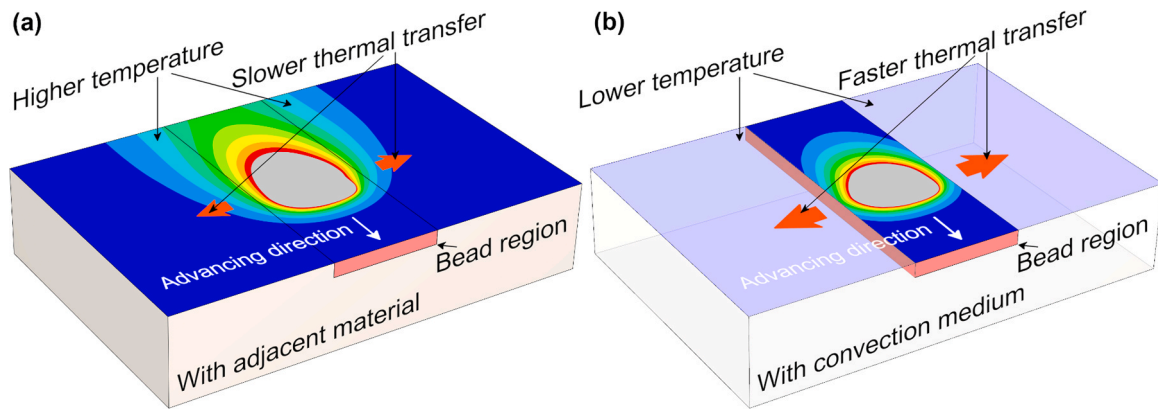


Fig. 3. Illustration of the difference between: (a) the heat conduction to the actual adjacent material, and (b) the heat convection to the imaginary convection medium through the interface boundaries surrounding the representative bead region of major interest for analysis.

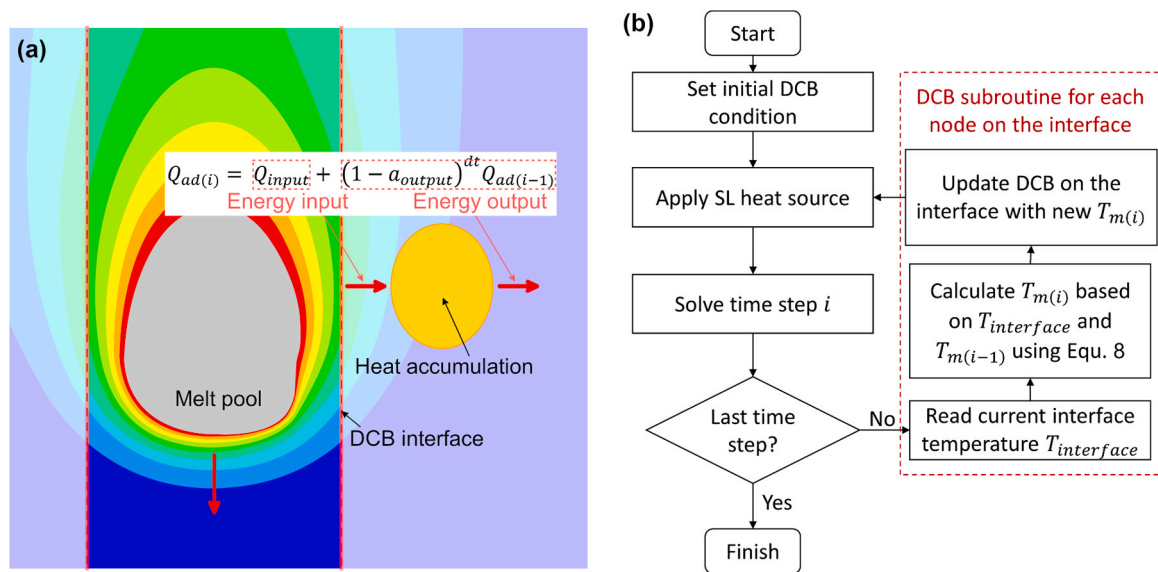


Fig. 4. (a) The principle of the DCB method, and (b) the flow chart of the subroutine to implement the DCB during the FE modelling.

1969). The expression of the Gaussian heat source model is given below:

$$Q(x, y) = \frac{3\eta Q_{total}}{\pi r^2} \exp\left[-3(x^2 + y^2)/r^2\right] \quad (9)$$

where Q represents the power density of the laser operative on a plane surface, Q_{total} represents the total laser power, x and y are the coordinates relative to the centre of the laser, r is a parameter that determines the radius of the heat source, and η is the laser energy absorptivity. Based on the defocused laser beam diameter, a radius parameter (r) of 2 mm was used. The laser absorptivity of the SL was calibrated using the experimental data, which was taken to be 55 % (shown in Section 3.1.1).

In addition to the Gaussian heat source for capturing the laser oscillation transients, a bar-shaped non-oscillating equivalent heat source was also introduced as a substitution for the SL heat source to further simplify the SL modelling. When the Gaussian heat source (as indicated in Eq. 9) oscillates with an infinitely high frequency, we can consider that the power of the heat source is evenly distributed in the crosswise direction and the oscillating Gaussian heat source reduces to a bar-shaped non-oscillating heat source. Eq. 10 expresses the equivalent SL heat source. The power at a specific position is integrated as the laser beam travels across it. Therefore, the power distribution of the equivalent heat source model can be calculated by the formula below:

$$Q_{equivalent}(x, y) = \int_{-w_s/2}^{w_s/2} \frac{3Q_{total} \exp\left\{-\frac{3[x^2 + (y-y')^2]}{r^2}\right\}}{\pi r^2 w_s} dy' \quad (10)$$

where $Q_{equivalent}$ is the bar-shaped non-oscillating equivalent heat source distribution, and w_s is the scanning width. The conversion of an oscillating laser beam profile to a non-oscillating bar-shaped equivalent heat source profile by Eq. 10 is illustrated in Fig. 5.

2.2.3. Modelling scheme

A sensitivity study on the dimensions of the full-scale thermal model was conducted to identify the appropriate width and thickness of the substrate for consideration in the FE modelling of the SL process. The dimensions of the tested full-scale models are listed in Table 2. Six width values with a constant thickness of 25 mm and three thickness values with a constant width of 132 mm were considered. The parameters used for the model sensitivity study were the same as the calibration experiment.

Based on the full-scale model size calibration (shown in Section 3.1.1), a full-scale model with dimensions of 132 mm × 60 mm × 25 mm was selected as the reference case for further FE modelling study, as shown in Fig. 6a. The representative bead region informed by the full-scale model was set to have dimensions of 17 mm × 60 mm

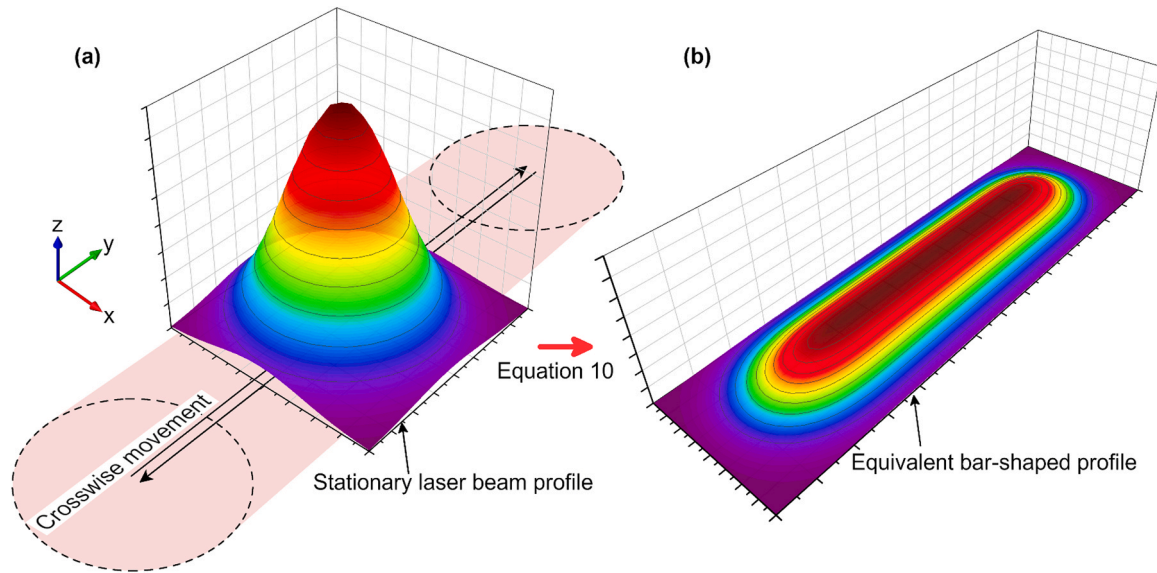


Fig. 5. Illustration of converting an oscillating SL beam profile to a non-oscillating bar-shaped equivalent heat source profile: (a) a stationary laser beam profile and its crosswise moving pattern, and (b) the converted equivalent heat source profile.

Table 2
Dimensions of the full-scale thermal models for the sensitivity study.

Varied width	Varied thickness
207 mm × 60 mm × 25 mm	132 mm × 60 mm × 25 mm
182 mm × 60 mm × 25 mm	
157 mm × 60 mm × 25 mm	132 mm × 60 mm × 20 mm
132 mm × 60 mm × 25 mm	
107 mm × 60 mm × 25 mm	132 mm × 60 mm × 15 mm
82 mm × 60 mm × 25 mm	

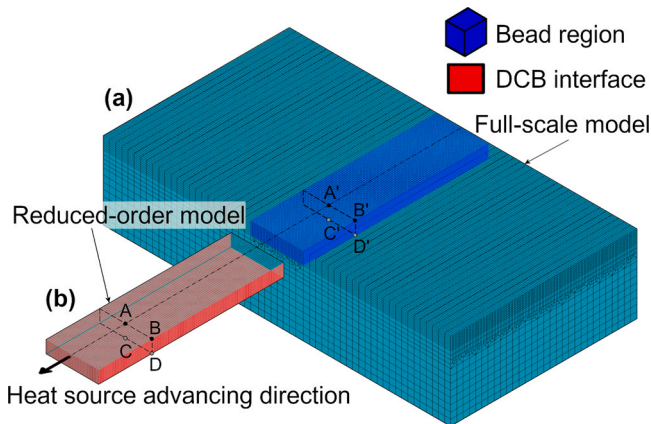


Fig. 6. FE meshes of: (a) the full-scale thermal model (inspection positions A'-D'), and (b) the reduced-order thermal model (inspection positions A-D).

× 4 mm, for which the element size is 0.5 mm, equal to 1/8 of the laser beam radius, to provide a sufficient resolution for the SL dynamic temperature field. The other region was meshed with an element size of 2 mm. Overall, 124,448 elements and 135,320 nodes were generated in the FE mesh.

A reduced-order thermal model with the bead region only was also built (Fig. 6b). The element size was set to be 0.5 mm, which is the same as the bead region in the full-scale model, resulting in 32,640 elements and 39,204 nodes. In the reduced-order model, the side surfaces and the bottom surface were applied with DCB interfaces, while the top, front and rear surfaces were applied with a constant convection coefficient to

represent the ambient air cooling. Another reduced-order model for comparison was generated by replacing the DCB interfaces with the traditional convection boundary condition that adopts a constant ambient temperature for the convection medium. Both reduced-order models were calibrated by fitting the temperature histories with the full-scale model results at the four inspected positions indicated in Fig. 6a and b. An oscillation frequency of 1.7 Hz was used for the calibration. An ambient air cooling convection coefficient of $5 \text{ W}/(\text{m}^2\text{K})$ was calibrated for the substrate surface based on the experimental results. The calibration of the reduced-order model was conducted separately using the full-scale model results, after which the DCB convection coefficient (h_{DCB}), energy input coefficient (a_{input}) and energy output coefficient (a_{output}) of the DCB were taken to be $15,000 \text{ W}/(\text{m}^2\text{K})$, 23 % per second and 0.4 % per second, respectively, and the convection coefficient for those surfaces on the regular reduced-order model was set to be $12,000 \text{ W}/(\text{m}^2\text{K})$. Both the initial and ambient temperatures for all the models were taken to be $45 \text{ }^\circ\text{C}$. The calibrations will be further discussed in Section 3.1.1. Pearson correlation coefficient (PCC) (Pearson, 1896) was calculated to evaluate the correlations of the temperature histories between the full-scale model and the DCB-based reduced-order model.

General purpose FE software ANSYS 2022R1 was employed to perform the modellings in a ThinkSystem SR645 server featuring an AMD EPYC 7543 32-core 2.8 GHz processor and 512 GB random access memory (RAM) for the computation. The computational time for the FE modellings using different models with different oscillation frequencies was recorded and compared (presented later).

2.2.4. Material properties

The material used in this study was S275 mild steel. The temperature-dependent material properties, including specific heat and thermal conductivity, were taken from Ref (Tan and Guo, 1994). The thermal properties of S275 mild steel in the model are listed in Table 3.

3. Results and discussion

3.1. Verification of the DCB-based reduced-order model

3.1.1. Model calibration

Fig. 7 shows the temperature histories at Position C' (indicated in Fig. 6a) of the full-scale thermal models with different widths (Fig. 7a)

Table 3
Dimensions of the models for the scale-sensitive study.

Parameters	Value
Density/(kg/m ³)	7820
Radiation emissivity	0.3
Solidus/(K)	1742
Liquidus/(K)	1785
Latent heat of melting/(J/kg)	2.6×10^5
Stefan-Boltzmann constant/(W/(m ² K ⁴))	5.67×10^{-8}
Specific heat/(J/(kgK))	Temperature-dependent (Tan and Guo, 1994)
Thermal conductivity/(W/(mK))	Temperature-dependent (Tan and Guo, 1994)

and thicknesses (Fig. 7b). In Fig. 7a, it can be seen that temperature history barely changed when the width was larger than 132 mm. When using a width smaller than 132 mm, the cooling of the substrate started to slow down. Fig. 7b further shows the variation of the temperature histories as a function of the thickness with a width of 132 mm. The temperature history is more sensitive to the substrate thickness than width.

The dimensions of the full-scale model determine the area of the ambient convection surfaces and the volume of the adjacent material surrounding the heat source, which are the two main factors affecting the cooling curve. The cooling rate would be lower without a sufficient surface area for ambient convection or a sufficient volume of adjacent material for conductive heat dissipation. Based on the results shown in Fig. 7, the dimensions of 132 mm × 60 mm × 25 mm were selected for the full-scale model in the following analysis.

The empirical parameters for Gaussian heat source and surface convection in the full-scale model with the selected dimensions were calibrated using the SL experiment data. Fig. 8 shows the comparison of the temperature histories at the four thermocouple locations (Fig. 1c) between the full-scale model predictions and the experimental measurements, which exhibit a close match and indicate good accuracy of the FE model. It is interesting to see that multiple temperature peaks appear in the predicted temperature history at Position 1, which are different to the single peak observed at the same position in the experiment. This could be attributed to the fact that the resolution of the thermocouple measurement is lower than the FE modelling, while the multiple peaks were attained in a short period of response time.

3.1.2. Determination of DCB parameters

The DCB parameters, including the DCB convection coefficient (h_{DCB}), energy input coefficient (a_{input}), and energy output coefficient (a_{output}), require iterative calibration, which is guided by theoretical estimates derived below.

Theoretically, Eqs. (3) and (4) can be combined when using a

convection interface to approximate thermal conduction. Therefore, the DCB convection coefficient (h_{DCB}) can be estimated as follows:

$$h_{DCB} = \frac{\lambda}{L} \quad (11)$$

where λ is the thermal conductivity of the substrate material, and L is the distance between the DCB interface and the “imaginary” nodes of the adjacent material. In this study, the element size of the adjacent material was 2 mm. If a constant thermal conductivity of 50 W/(mK) is given, an estimated DCB convection coefficient h_{DCB} of 25000 W/(m²K) can be calculated accordingly.

Within each time step, the temperature difference between the DCB interface and the adjacent material (Eq. (7)) is reduced. Therefore, an energy input coefficient (a_{input}) with a value less than 1 needs to be set to compensate for the reduction of the energy input (Q_{input}) caused by the decrease in the temperature difference. It is worth pointing out that the energy input coefficient (a_{input}) and the DCB convection coefficient (h_{DCB}) are correlated. A longer “imaginary” distance (L) represents a smaller change in the temperature difference within each time step and, therefore, a higher energy input coefficient (a_{input}). However, the DCB convection coefficient (h_{DCB}) would be lower according to Eq. (11). These two parameters should be adjusted accordingly during the calibration.

The theoretical estimate of the energy output coefficient (a_{output}) assumes that the heat input from the heat source was uniformly distributed over the substrate instantly, and then the temperature rise can be calculated by:

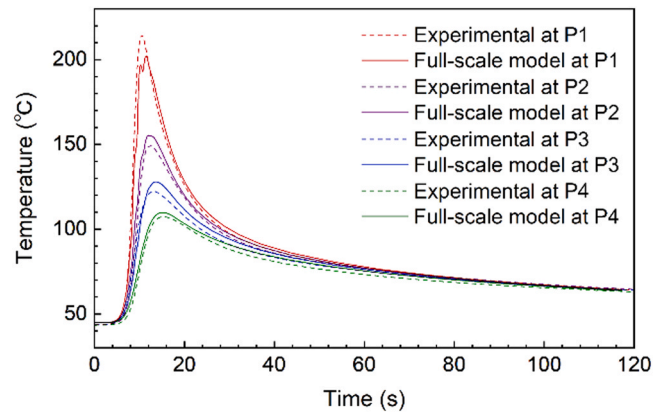


Fig. 8. Comparison between the full-scale thermal model and the thermocouple measurement results at the four positions indicated in Fig. 1c.

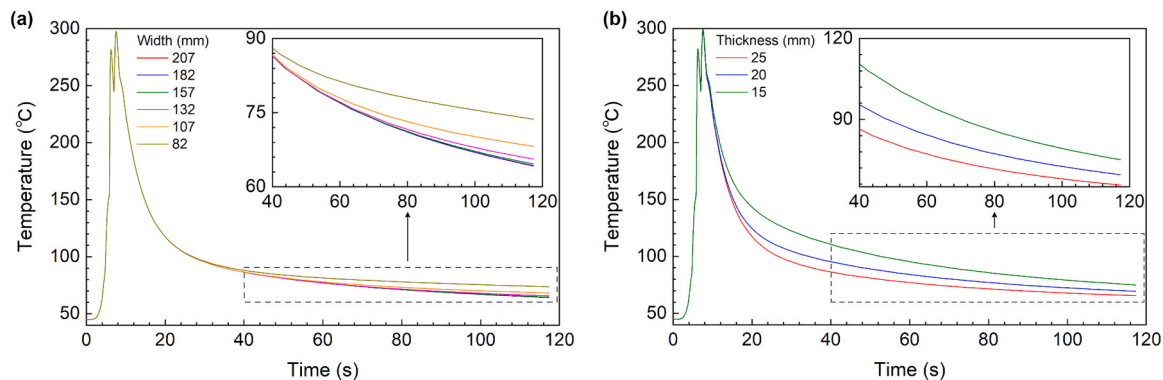


Fig. 7. Results of the dimension sensitivity study of the full-scale model. Temperature histories at Position C' are compared: (a) with varied widths and a thickness of 25 mm, and (b) with varied thicknesses and a width of 132 mm.

$$\Delta T = \frac{\eta Q_{total}}{vtHW\rho C} \quad (12)$$

where ΔT is the temperature rise of the substrate, t is the time, Q_{total} represents the total laser power, η is the laser energy absorptivity for the substrate, ρ is the density, C is the specific heat, v is the advancing speed of the heat source, and H and W are the thickness and width of the substrate, respectively. The heat lost (Q_{output}) transferred by the ambient air convection can be then calculated by:

$$Q_{output} = hA\Delta T = h \cdot 2vtW \cdot \frac{\eta Q_{total}}{vtHW\rho C} = 2h \frac{\eta Q_{total}}{H\rho C} \quad (13)$$

where h is the convection coefficient of the ambient air, and A is the area of the top and bottom surfaces of the substrate. So, the energy output coefficient (a_{output}) under this circumstance can be calculated:

$$a_{output} = \frac{Q_{output}}{\eta Q_{total}} = \frac{2h}{H\rho C} \quad (14)$$

Given an ambient convection coefficient (h) of 5 W/(m²K), and specific heat (C) of 500 J/(kgK), an energy output coefficient (a_{output}) of about 0.01 % is given. This value is calculated with the assumption of infinitely fast thermal conduction within the substrate. However, the heat loss would be higher due to a greater temperature difference near the heated area during the SL modelling. Consequently, the value calculated by Eq. (14) is the minimum value of the energy output coefficient (a_{output}). A value higher than the estimated minimum value of 0.01 % should be given during the iterative calibration.

Starting with the theoretically estimated values of the empirical parameters, the DCB method was calibrated using the full-scale model results, and then the energy input coefficient (a_{input}), energy output coefficient (a_{output}), and DCB convection coefficient (h_{DCB}) were obtained after several rounds of trials. Fig. 9 shows the variation in the temperature history as a function of the a_{input} , a_{output} and h_{DCB} . Fig. 9a shows the temperature histories at Position C (indicated in Fig. 6b) with varying

a_{output} . It can be observed that the a_{output} only affects the temperature change at the cooling stage. A lower a_{output} represents that more energy is preserved after each time step, leading to a slower cooling speed. Fig. 9b and c show that both a_{input} and h_{DCB} affect the peak temperature at the heating stage. The time interval between two laser interactions at the edge of the scanning width is about 0.6 s. The temperature dropped between the two interactions, which led to multiple temperature peaks. The deviation at the second peak, as shown in Fig. 9b, is slightly larger than that at the first peak when varying a_{input} . This is because the a_{input} determined the heat accumulation effect, and as a result, the deviation changed with time. When applying different h_{DCB} , however, the deviations of two peaks are similar, since the h_{DCB} only affected the overall cooling trend. The DCB condition was calibrated by adjusting the above-mentioned three parameters to fit the peak temperature and cooling rate obtained from the full-scale model.

3.1.3. Verification by the full-scale model

Fig. 10 shows the predicted temperature distributions in the top view (Fig. 10a–c) and cross-section view (Fig. 10d–f) for three different models. Overall, the predictions by the DCB-based reduced-order model matched the full-scale model in the bead region, while the reduced-order model without DCB led to a more concentrated temperature distribution. This indicates that the reduced-order model with DCB is more effective in representing the full-scale model.

Fig. 11 further shows the distributions of the derived thermal gradients for the three different models. The thermal gradient (T') is defined in Eq. (15):

$$T' = \sqrt{\left(\frac{\partial T}{\partial x}\right)^2 + \left(\frac{\partial T}{\partial y}\right)^2 + \left(\frac{\partial T}{\partial z}\right)^2} \quad (15)$$

where T is the temperature distribution as a function of position and time, and x , y , and z are the coordinates. The numerical algorithm for obtaining the full-field distribution of thermal gradient is described in

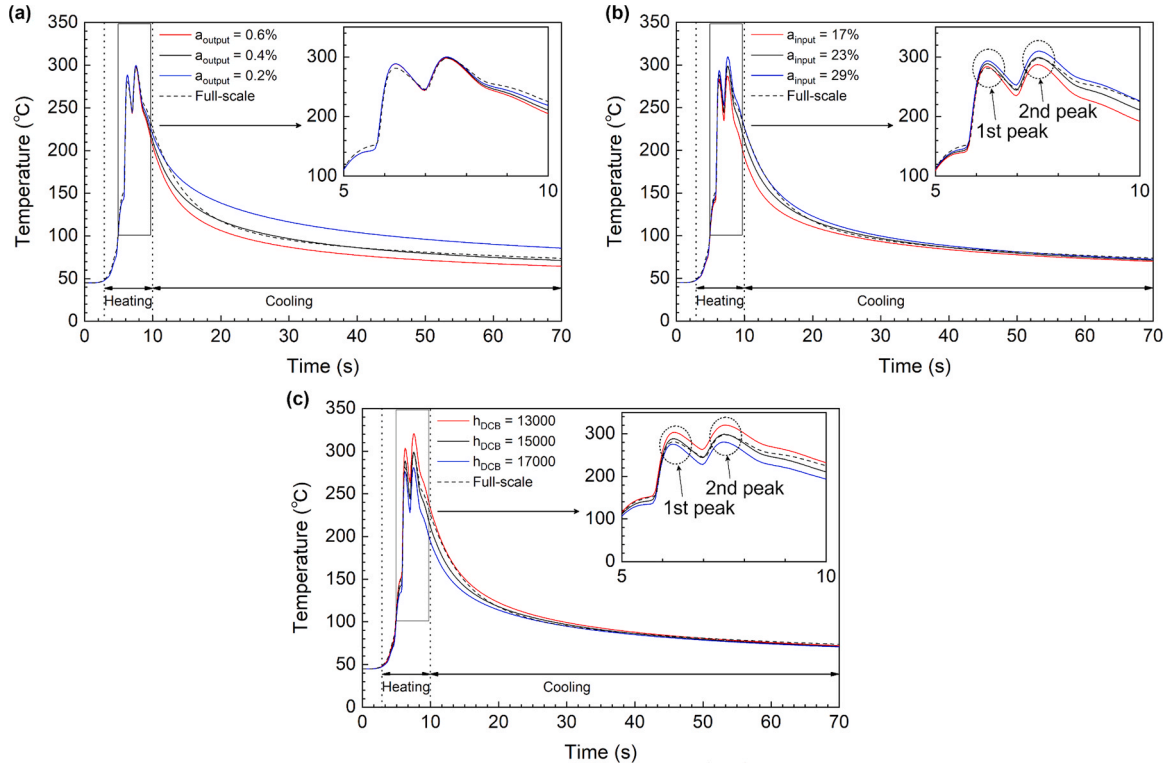


Fig. 9. Temperature histories at Position C (indicated in Fig. 6b) when varying DCB parameters including: (a) energy output coefficient (a_{output}), (b) energy input coefficient (a_{input}), and (c) DCB convection coefficient (h_{DCB}).

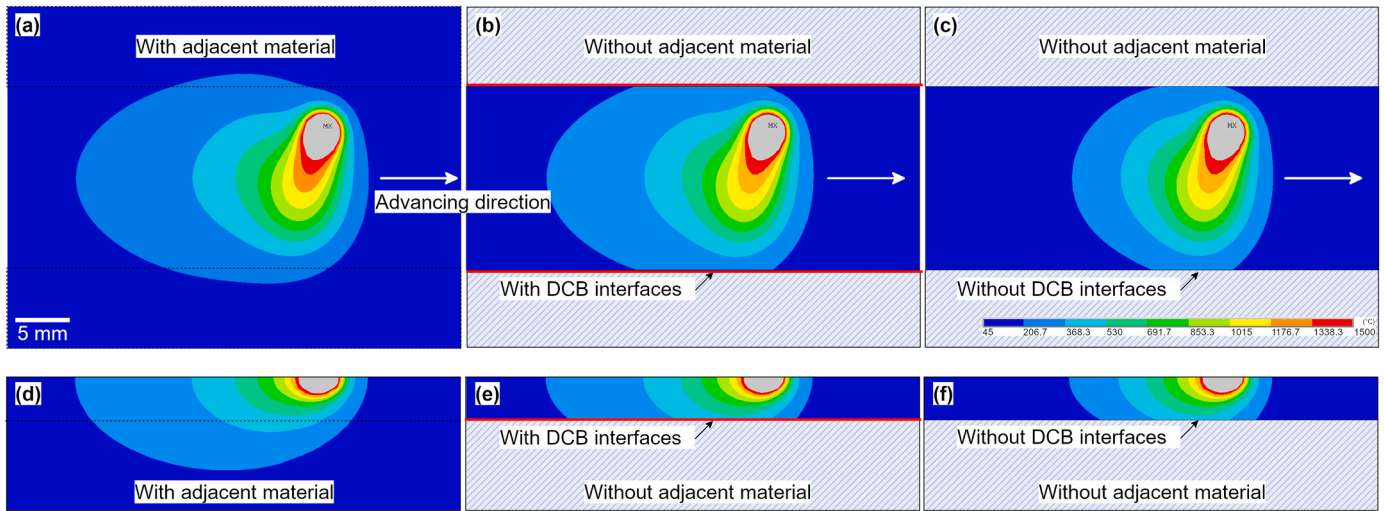


Fig. 10. Top: top views of the temperature distributions predicted by three models with laser beam located at the oscillation path edge: (a) full-scale model, (b) reduced-order model with DCB, and (c) reduced-order model without the DCB; Bottom: cross-section views along the laser advancing direction: (d) full-scale model, (e) reduced-order model with DCB, and (f) reduced-order model without DCB.

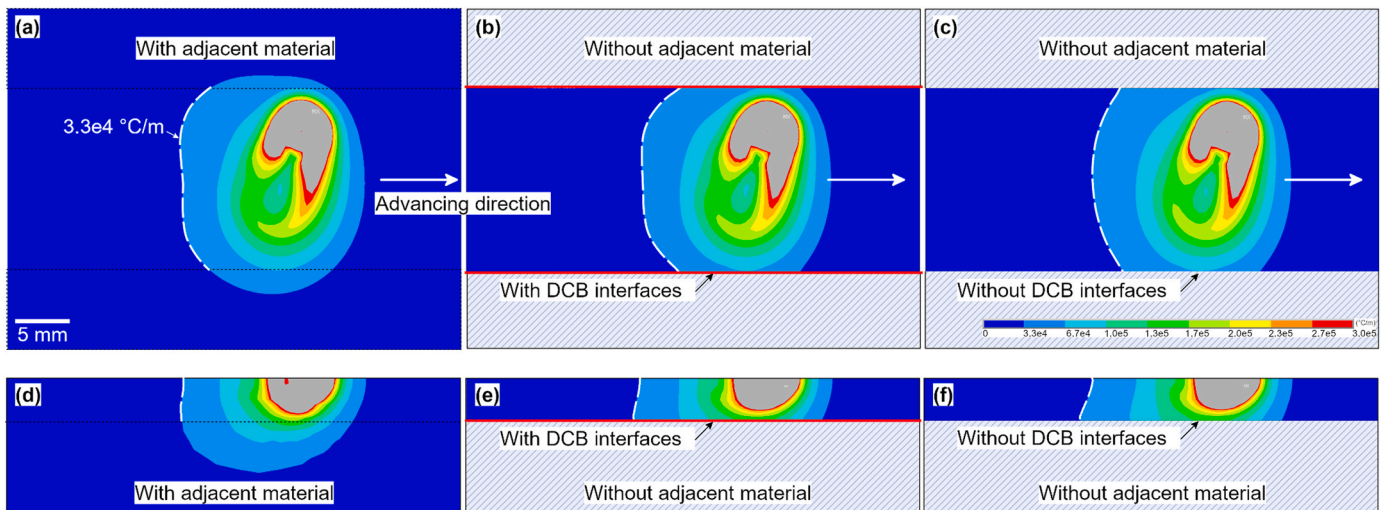


Fig. 11. Top: top views of the thermal gradient distributions predicted by the three models with laser beam located at the oscillation path edge: (a) full-scale model, (b) DCB-based reduced-order model, and (c) reduced-order model without DCB; Bottom: cross-section views along the laser advancing direction: (d) full-scale model, (e) DCB-based reduced-order model, and (f) reduced-order model without DCB.

Ref. Wang et al. (2022). Despite the similarity of the thermal gradient contours near the heat source centre, the reduced-order model without DCB predicted markedly different thermal gradient contours in a lower temperature range relatively far from the heat source centre, e.g., the contours with a thermal gradient of 3.3×10^4 °C/m (indicated as white dashed lines in Fig. 11). From the comparisons shown in Figs. 10 and 11, it is evident that the DCB-based reduced-order model can reproduce the distributions of temperature and its gradient that are predicted by the full-scale model.

Fig. 12 shows the temperature histories at the four positions indicated in Fig. 6b, which were obtained from the full-scale model and the reduced-order models with and without the DCB. A major difference is that the cooling curve of the reduced-order model without DCB drops significantly faster than those of the other two models, while the temperature histories of the full-scale model and the reduced-order model with DCB are well-matched at all four positions.

Besides the overall cooling trends, the temperature variations around the local peak temperatures are also examined for different positions. PCC of the temperature histories between the full-scale model and

reduced-order models within the period of 2–17 s were calculated (annotated in Fig. 12 as r). This period includes the most rapid temperature changing of the model and can provide critical information for both process and material analysis. The accuracy within this period is therefore representative. When the heat source oscillated, the effect of the thermal conduction by the adjacent region on Positions A and B (located on the top surface near the heat source) was less significant than on Positions C and D (located on the bottom surface relatively far from the heat source). For instance, in Fig. 12a and b, the temperature variations near the local peak are similar for all three models, while in Fig. 12c and d the three models predicted similar first temperature peaks but the reduced-order model without DCB predicted markedly lower levels of the second peak temperature. Both the DCB-based and non-DCB reduced-models show high correlations to the full-scale model at Positions A and B where temperatures were dominated by the heat source. The correlations of the DCB-based model are slightly higher than those of the non-DCB reduced-model. However, the correlation non-DCB reduced-order model deviated from the full-scale model dramatically at Positions C and D where temperatures were dominated by thermal

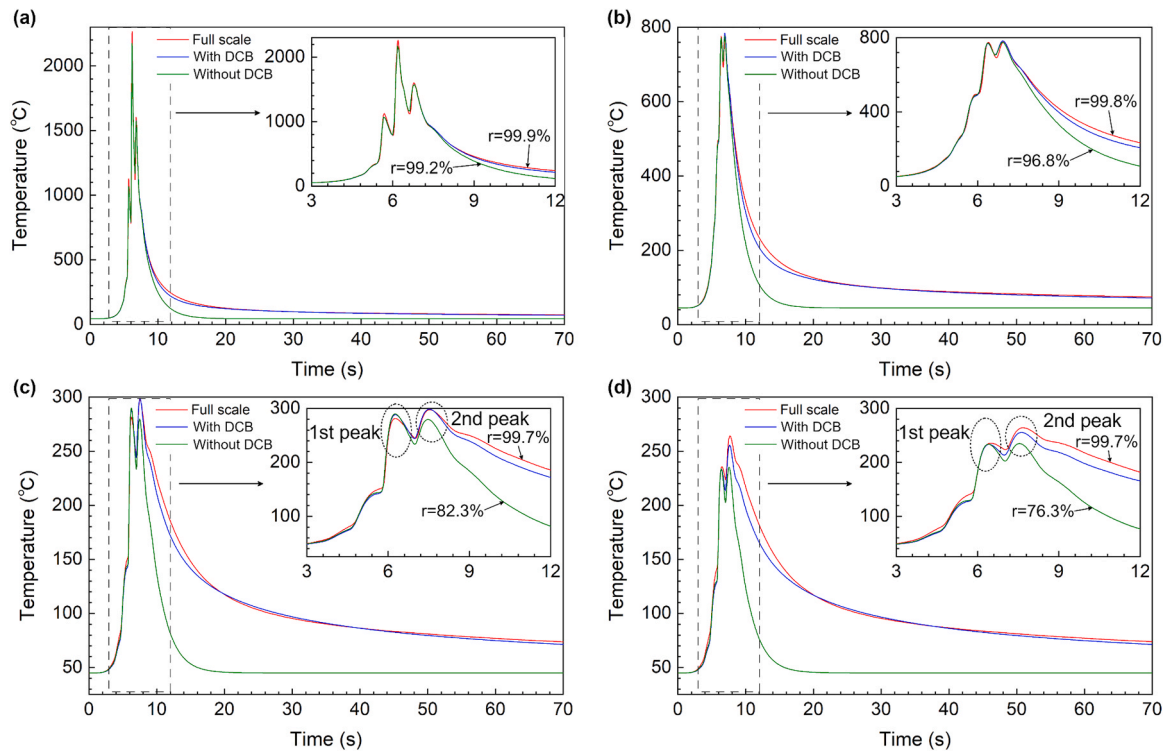


Fig. 12. Comparison of the predicted temperature histories at the four positions indicated in Fig. 6b among three models: (a) Position A, (b) Position B, (c) Position C, and (d) Position D.

conduction, and the correlation dropped from 99 % to respectively 82.3 % and 76.3 %. On the contrary, the correlation of the DCB-based reduced-order to the full-scale model was kept above 99.7 % at all four positions. It is evident that the DCB method not only improved the reduced-order model for predicting the cooling stage but also successfully simulated the detailed thermal response that is representative for the full-scale model with over 99 % accuracy.

3.2. Reduced-order thermal modelling of a SL process

3.2.1. Effect of oscillation frequency on melt pool geometry

Fig. 13 shows the predicted thermal contour results of the SL process with different oscillation frequencies when the DCB-based reduced-

order model was employed. In the coloured maps, the grey region outlines the area with a temperature exceeding 1500 °C, which is approximately the melting point of the steel and hence the isothermal line represents the melt pool shape. The melt pool can be observed as an oval shape with a lower oscillation frequency of 1.7 Hz. The shape of the melt pool changed when the laser beam moved across the scanning width. As the oscillation frequency increased, the melt pool shape changed to a symmetric triangle with rounded corners. The dynamic changing of the melt pool shape was gradually eased. The melt pool turned into a consistent shape when the oscillation frequency increased to 13.6 Hz and higher values. Xia et al. (2022) compared the thermal profile of a circular oscillating laser and a traditional Gaussian laser for a nickel-based superalloy deposition process. Different oscillating laser

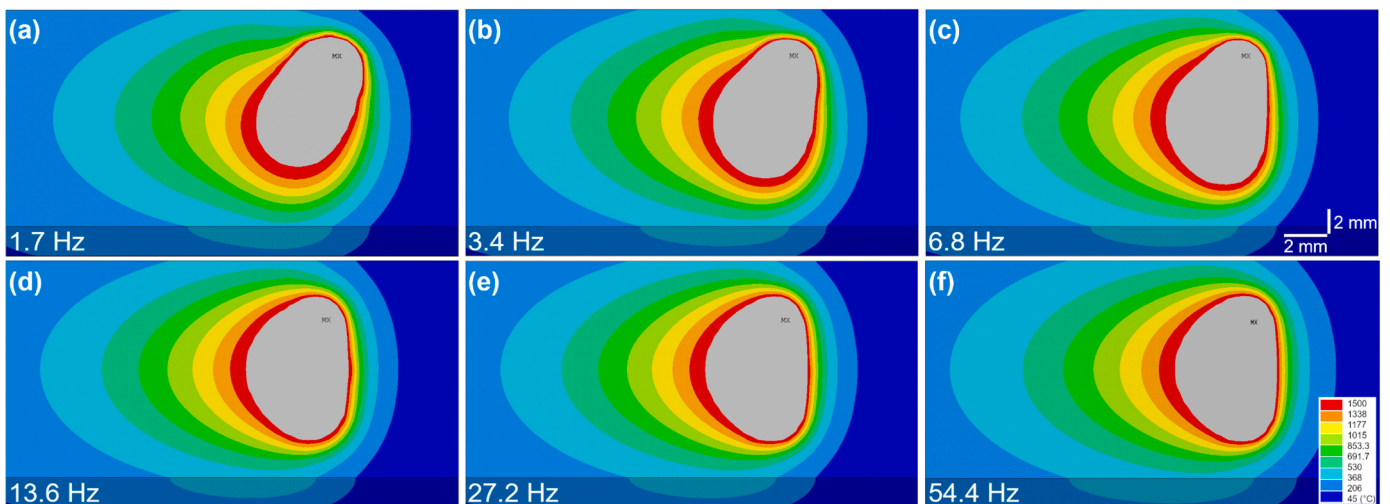


Fig. 13. Predicted temperature contours in the top view for the DCB-based reduced-order thermal model with different oscillation frequencies (the laser beam is located at the side): (a) 1.7 Hz, (b) 3.4 Hz, (c) 6.8 Hz, (d) 13.6 Hz, (e) 27.2 Hz, and (f) 54.4 Hz.

with oscillation frequency varied from 5 to 100 Hz was tested. In their study, the results showed that the thermal profile of the oscillating laser reached a continuous state with an oscillation frequency of 30 Hz and higher, which agrees with the results shown in Fig. 13.

Fig. 14 shows the thermal images of the SL melt pool with different oscillation frequencies. When the steel substrate was melted, the reflectance of the surface rose dramatically, and the emissivity dropped rapidly. As a result, the melting pool in the thermal images was detected as a dark area surrounded by the highlighted contour (Kim and Feng, 2016). The melt pool shapes observed in the thermal images match the modelling result (Fig. 13), which are manifested as the same consistent symmetric triangle with rounded corners for an oscillation frequency of 13.6 Hz.

In certain applications such as the MES AM process, SL is featured as a reshaping heat source. A stable melt pool with minor temperature fluctuation and melt pool shape-changing is sought for accurate deposition. In the case of our study, the melt pool shape was stabilized with a low oscillation frequency, indicating that the SL-based AM process is feasible for industrial applications. The DCB-based reduced-order thermal model accurately predicted the SL melt pool shape, which is essential for the study of the SL-assisted AM process.

Fig. 15 compares the cross-sections between the modelling and experimental results. The fusion line in the modelling result can be represented by the thermal contour of the melting temperature. The grey area when the temperature exceeds the melting point represents the melt pool shape. By comparing the thermal contour result with the cross-section macrograph side-by-side, it can be seen that the predicted depth and shape of the melt pool are in good agreement with the experimental result. This further confirmed that the modelling has a high prediction accuracy for both melt penetration and expansion.

3.2.2. Effect of oscillation frequency on thermal variables

The thermal characteristics, including the heating rate, cooling rate and thermal gradient, are the essential factors that determine the metallurgical and mechanical quality of AM products (Cao et al., 2023). In this section, the DCB-based reduced-order model was used for the study of the effect of oscillation frequency on the thermal characteristics of the SL process.

Figs. 16 and 17 show the distributions of the derived thermal gradients in the top view for the SL with different oscillation frequencies when the laser beam is positioned at the edge and the middle of the oscillation amplitude, respectively. For a low oscillation frequency of 1.7 Hz, the distributions of the thermal gradients are in an asymmetric shape that altered when the laser beam scanned from the edge to the

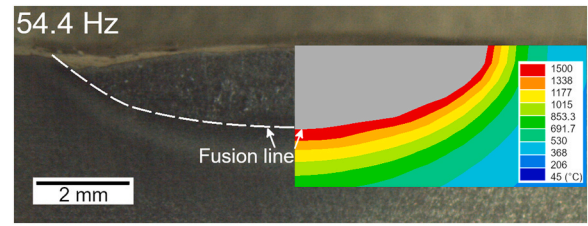


Fig. 15. Comparison between the modelling and experimental results for a transverse cross-section.

middle. These results indicate a lack of steady condition of the low oscillation frequency SL in terms of thermal gradients in the heated area. When increasing the oscillation frequency from 1.7 Hz to 54.4 Hz, the asymmetry of the thermal gradient is reduced, and a consistent shape was formed. By comparing the thermal gradient distributions of the SL process with different laser beam locations, it can be seen that the effect of the laser beam movement on the thermal gradient distribution was significantly reduced with a higher oscillation frequency, which further indicates that the consistency of the SL thermal characteristics was enhanced.

The temperature variation rate (\dot{T}) is defined below:

$$\dot{T} = \frac{\partial T}{\partial t} \quad (16)$$

where T is the temperature at the inspected position and time, and t is the time. The positive and negative values of \dot{T} represent heating and cooling rates, respectively. The instantaneous temperature variation rates at Positions B and D (indicated in Fig. 6b) with varied oscillation frequencies are obtained and plotted in Fig. 18. Multi-peak waveform temperature variation rate profiles are found with low oscillation frequencies (1.7, 3.4 and 6.8 Hz). The great amplitude of the temperature variation rate waveform of the low oscillation frequency SL process implies massive changes in the thermal condition. As the oscillation frequency increased, the temperature variation rate curve was smoothed and eventually converged into a single-peak curve. This is evidence that a higher oscillation frequency can avoid rapid temperature shifting caused by the crosswise movement of the laser beam heat source.

3.2.3. Prediction by non-oscillating equivalent heat source

The bar-shaped equivalent heat source was then applied to the DCB-based reduced-order thermal model to verify its capability as an approximate substitute for a high-frequency oscillating SL heat source.

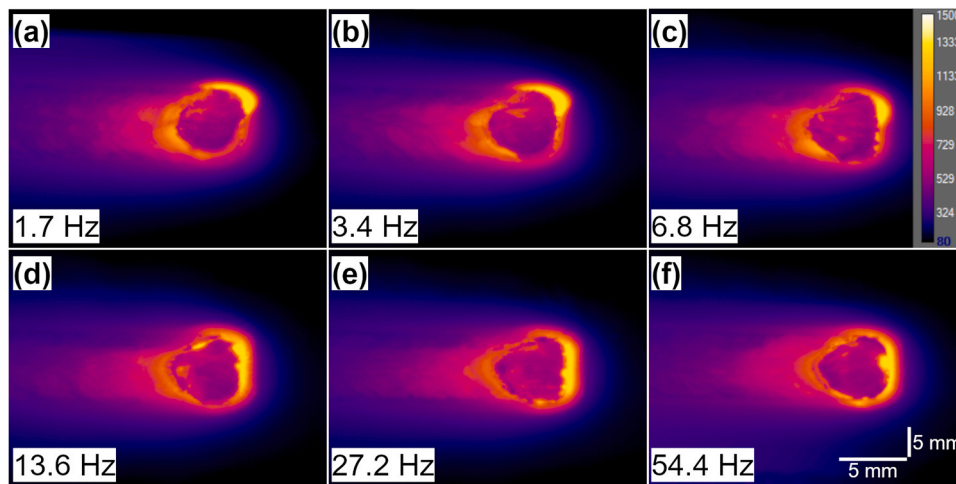


Fig. 14. Thermal images of the SL melt pools with different oscillation frequencies (the laser beam is located at the side): (a) 1.7 Hz, (b) 3.4 Hz, (c) 6.8 Hz, (d) 13.6 Hz, (e) 27.2 Hz, and (f) 54.4 Hz.

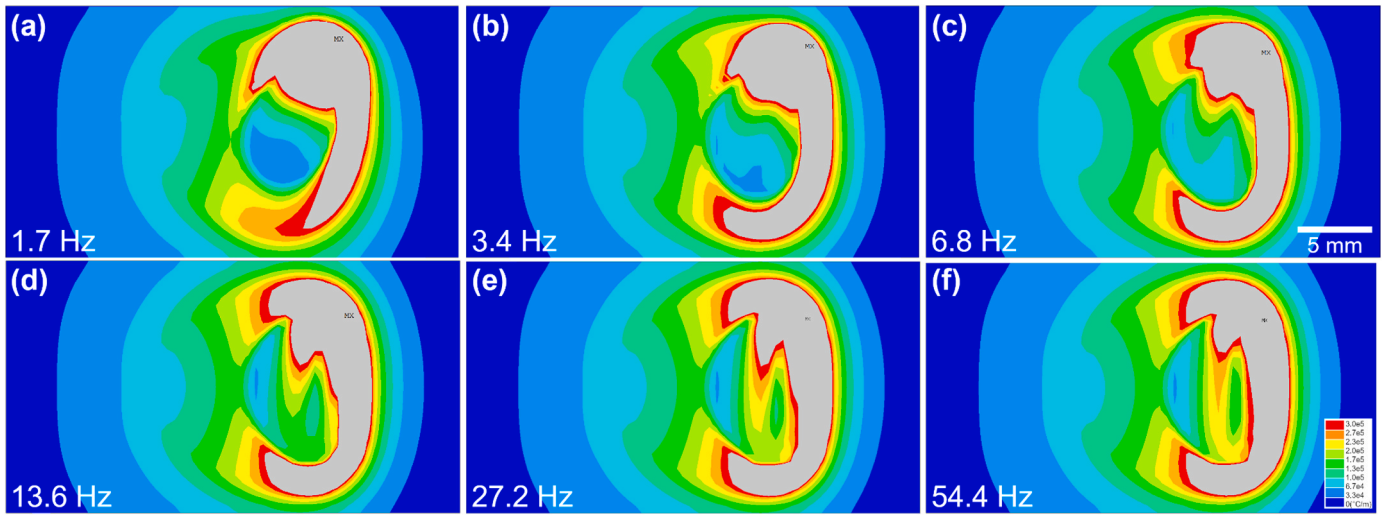


Fig. 16. Predicted thermal gradient contours in the top view for the DCB-based reduced-order thermal model with different oscillation frequencies (the laser beam is located at the side): (a) 1.7 Hz, (b) 3.4 Hz, (c) 6.8 Hz, (d) 13.6 Hz, (e) 27.2 Hz, and (f) 54.4 Hz.

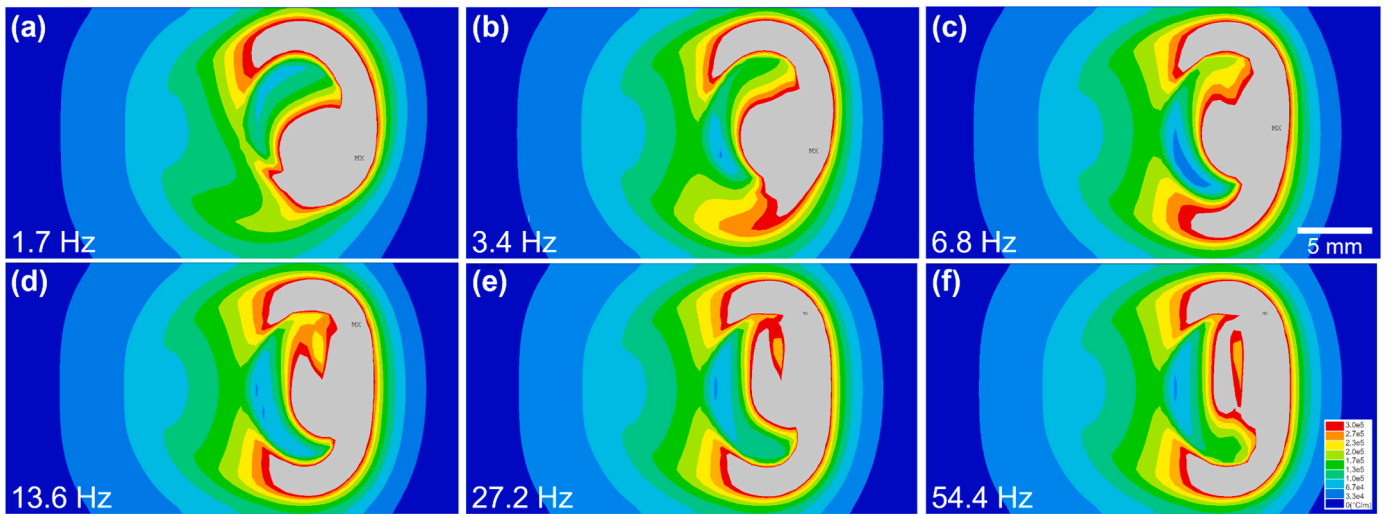


Fig. 17. Predicted thermal gradient contours in the top view for the DCB-based reduced-order thermal model with different oscillation frequencies (the laser beam being located at the middle): (a) 1.7 Hz, (b) 3.4 Hz, (c) 6.8 Hz, (d) 13.6 Hz, (e) 27.2 Hz, and (f) 54.4 Hz.

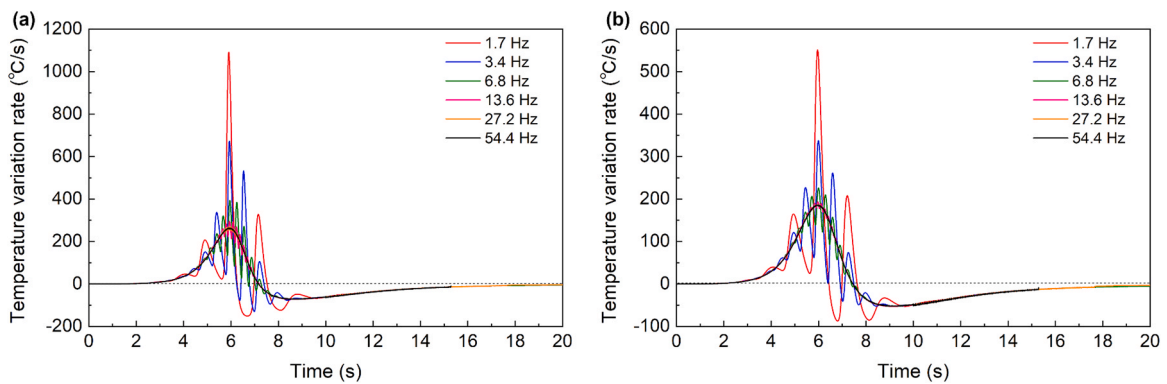


Fig. 18. Instantaneous temperature variation rate determined from the DCB-based reduced-order thermal model at Positions B and D (Fig. 6b): (a) Position B, and (b) Position D. Note that the positive and negative values indicate heating and cooling, respectively.

Fig. 19 compares the thermal results of the 54.4 Hz oscillating SL heat source and the bar-shaped equivalent heat source. The melt pool shape of the 54.4 Hz oscillating SL is highly similar to that of the bar-shaped

equivalent heat source. This indicates that the bar-shaped equivalent heat source can ensure sufficient prediction accuracy when the laser oscillation frequency is high.

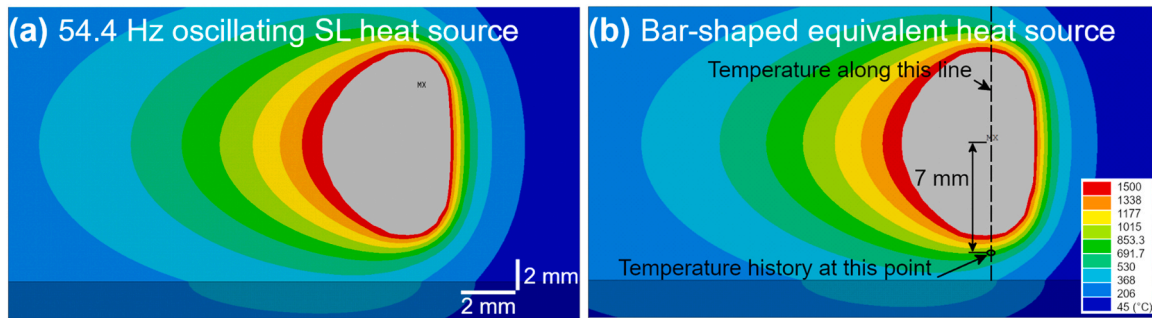


Fig. 19. (a) Comparison of the melt pool shape between: (a) 54.4 Hz oscillating SL heat source, and (b) non-oscillating bar-shaped equivalent heat source.

To further analyze the consistency between the oscillating SL heat source and the non-oscillating bar-shaped equivalent heat source, more temperature data was extracted from the models. The temperature distributions of the melt pool along the scanning width when the laser beam reached the edge of the SL are plotted in Fig. 20a, and the temperature histories at the edge of the SL (indicated in Fig. 19b along with the bar-shaped heat source thermal contour) are compared in Fig. 20b. In Fig. 20a, the black curve represents the temperature distribution across the bar-shaped equivalent heat source, and the coloured lines represent the temperature distribution of the SL with different oscillation frequencies. A dashed line was drawn to represent the melting point of steel and helps indicate the width of the melt pool. As the oscillation frequency increases, the temperature distribution along the crosswise direction changes from an asymmetric shape to a symmetric shape. The region above the dashed line was skewed to the side when applying a lower oscillation frequency and was centralized when increasing the oscillation frequency. The temperature distributions of the SL with an oscillation frequency higher than 13.6 Hz resemble the temperature distribution of the bar-shaped equivalent heat source, further indicating that the thermal solution associated with the bar-shaped equivalent heat source is similar to that of a quasi-steady single-direction moving heat source.

Fig. 20b plots the temperature history at the edge of melt pools for the oscillating SL heat sources and non-oscillating bar-shaped equivalent heat source. It is seen that the temperature history exhibited multi-peak waving forms. Li and Gu (2014) developed a three-dimensional thermal model for selective laser melting (SLM) and studied the effects of scan speed and laser power on SLM thermal behaviour. The temperature history they presented in their study showed similar fluctuations with multiple peaks representing the arrival of the laser beam, which matches the results shown in Fig. 20b. The number of peaks increased with the oscillation frequency while the fluctuation was gradually eased. The curves were smoothed and eventually converged to the temperature history of the bar-shaped equivalent heat source. Especially, when the

oscillation frequency was above 13.6 Hz, the temperature history of the oscillating SL shows minor deviations from the bar-shaped equivalent heat source. Based on these results, the capability of using a bar-shaped equivalent heat source as a simplified substitution for a high-frequency oscillating SL heat source is verified.

3.3. Computational efficiency

The computational time of the SL modelling was recorded and compared to determine the computational efficiency of the different models. In this study, the number of timesteps required for the modelling of the SL with different oscillation frequencies was not consistent. 600 timesteps were computed for both the full-scale model and the reduced-order models when modelling the 1.7 Hz SL. The travel distance of the laser beam was kept constant for different oscillation frequencies, so the accumulated length of the scanning path increased with the oscillation frequency proportionally. As a result, the number of timesteps is a linear function of the oscillation frequency with a constant moving increment. Correspondingly, the number of timesteps ranged from 600 to 19,200 when increasing the oscillation frequency from 1.7 Hz to 54.4 Hz.

Fig. 21 shows the total computational time of the full-scale models and DCB-based reduced-order models with different oscillation frequencies. The total computational time is determined by the computational time per timestep and the number of the timesteps. For the same model, the computational time per step was approximately the same. Therefore, the total computational time is a linear function of the oscillation frequency, which is shown in Fig. 21. The total computational time of the DCB-based reduced-order models is about 42 % of that of the full-scale models for all oscillation frequencies, indicating that the reduced number of elements, as enabled by the DCB, has significantly accelerated the computation of the modelling. The dashed line across the diagram in Fig. 21 is the computational time of the DCB-based reduced-order model with the non-oscillating equivalent heat source

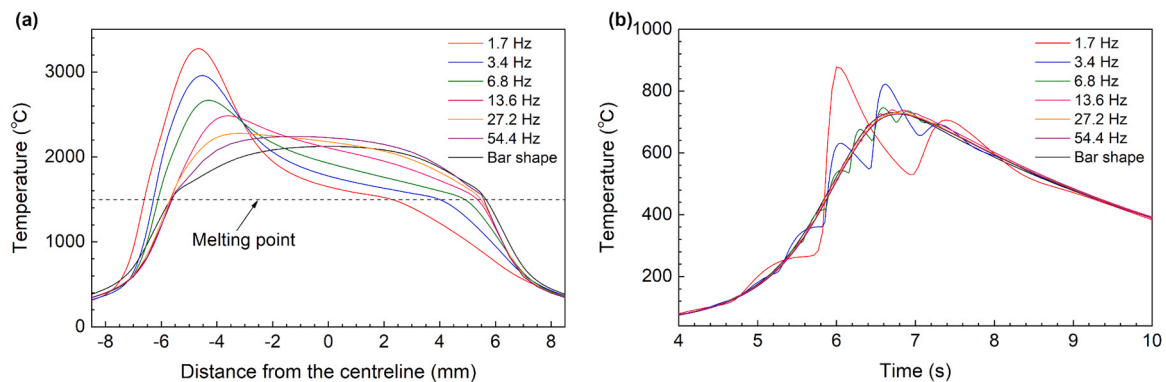


Fig. 20. (a) Temperature distribution in the melt pool across the scanning width, and (b) temperature histories at the edge of the SL source 7 mm away from the centre line.

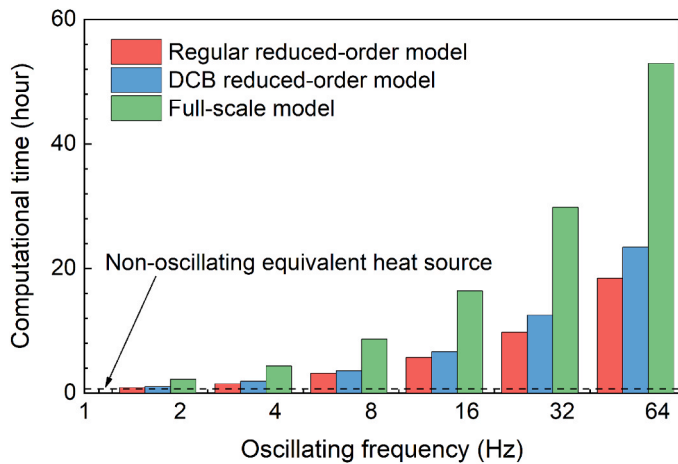


Fig. 21. The computational time vs. oscillation frequency for the full-scale model and the reduced-order models.

using the same timestep as the 1.7 Hz oscillating SL heat source for comparison. With the same timestep, the computational time of the equivalent heat source is 8 % lower than the 1.7 Hz oscillating SL heat source. However, such a fine time resolution is normally not required for the non-oscillating heat source. A larger timestep could be adopted in future work for the study of the SL using the non-oscillating equivalent heat source to further accelerate the computation.

The computational time of the reduced-order models with the regular interface is about 85 % of that of the DCB models, meaning the computation of the DCB subroutine took about 15 % of the computational time. In this study, the DCB subroutine was programmed using APDL macro script of ANSYS software. The computational efficiency of the macro script is essentially lower than the solver. As a result, the computational time of the subroutine took a noticeable amount of the total computational time. In future studies, the subroutine could be integrated into the solver to further accelerate the computation.

Based on the above analysis, the results show that the DCB-based reduced-order model can significantly improve computational efficiency for thermal analysis.

4. Further considerations

In this study, the DCB method was proposed, and the reduced-order thermal model with fewer elements successfully accelerated the computation without sacrificing prediction accuracy. However, the iterative function of the DCB that approximates the adjacent material temperature was determined by calibration. This iterative function is related to many characteristics of the substrate, such as substrate scale, material properties, room temperature, convection coefficient of ambient cooling, etc. Future studies could focus on the analysis of the relationships between these characteristics and the iterative function of the DCB, and establishing empirical equations for determining the DCB parameters, which is essential for the practical applications of the DCB method.

The DCB-based reduced-order model is a simplification of a large simple structure focusing on the thermal analysis of the heated regions. For complex structures, different intersections could be categorized and assigned with different DCBs accordingly. Adequate research on the categorization of different intersections is indispensable to make this technique feasible for a wider range of applications.

In the future numerical study on the SL-assisted AM process with high oscillation frequency, the bar-shaped equivalent heat source model can be applied to represent the quasi-steady-state SL as a layer-shaping heat source in the MES system. The transient thermal model of the MES process could be therefore replaced by a steady-state thermal model

which is much more computationally efficient (Ding et al., 2011). The application of the bar-shaped equivalent heat source in thermal analysis could efficiently assist the design of MES-based AM processes.

5. Conclusions

In this study, an innovative DCB method was proposed to enable the development of a reduced-order thermal model with a smaller problem domain and accelerate the modelling of the SL for the AM process. Furthermore, a non-oscillating bar-shaped equivalent heat source was introduced as a simplified substitution for the high oscillation frequency SL heat source to further enhance the modelling efficiency. The following conclusions are drawn:

1. The DCB method can approximate the thermal conduction of the adjacent material around the bead region for a reduced-order thermal model with over 99 % prediction accuracy compared to a full-scale model.
2. The DCB method reduces the problem domain and the number of elements for the SL process modelling which is computationally demanding due to the heat source oscillation, and thereby improves the computational efficiency. For the specific SL process considered in this study, the DCB method reduced the element amount reduced by 73 %, and computational time by 58 %.
3. The thermal analysis of the SL processes using the DCB-based reduced-order thermal model showed that an oscillation frequency higher than 13.6 Hz can contribute to a stable SL melt pool with a relatively symmetric thermal gradient and smooth temperature variation rate.
4. Both the experimental and numerical results show that the non-oscillating equivalent bar-shaped heat source model can be used as a substitution for the oscillating SL heat source model with an oscillation frequency higher than 13.6 Hz.

CRedit authorship contribution statement

Guangyu Chen: Conceptualization, Methodology, Software, Formal analysis, Investigation, Writing – original draft, Visualization. **Jialuo Ding:** Methodology, Investigation, Writing – review & editing, Supervision, Project administration. **Yongle Sun:** Methodology, Investigation, Writing – review & editing. **Xin Chen:** Methodology, Investigation, Writing – review & editing. **Chong Wang:** Investigation, Writing – review & editing. **Goncalo Rodrigues Pardal:** Investigation. **Stewart Williams:** Resources, Writing – review & editing, Supervision, Funding acquisition.

Declaration of Competing Interest

The authors declare the following financial interests/personal relationships which may be considered as potential competing interests: Guangyu Chen report financial support was provided by China Scholarship Council. Stewart Williams reports financial support was provided by Engineering and Physical Sciences Research Council.

Data Availability

Data underlying this study can be accessed through the Cranfield University repository at <https://doi.org/10.17862/cranfield.rd.24191241>.

Acknowledgement

Guangyu Chen would like to express his gratitude to Cranfield University, UK and China Scholarship Council, China (No. 201706680064) for funding his research studies. The authors would like to thank NEWAM (EP/R027218/1) program for financial support. The authors

also would like to thank Dr. Wojciech Suder, Dr. Sonia Martins Meco, Flemming Nielsen, Nisar Shah and John Thrower for their academic and technical support.

References

- Basak, A., Acharya, R., Das, S., 2016. Additive manufacturing of single-crystal superalloy CMSX-4 through scanning laser epitaxy: computational modeling, experimental process development, and process parameter optimization. *Metall. Mater. Trans. A Phys. Metall. Mater. Sci.* 47 <https://doi.org/10.1007/s11661-016-3571-y>.
- Cao, Q., Zeng, C., Qi, B., Jiang, Z., Zhang, R., Wang, F., Cong, B., 2023. Excellent isotropic mechanical properties of directed energy deposited Mg-Gd-Y-Zr alloys via establishing homogeneous equiaxed grains embedded with dispersed nano-precipitation. *Addit. Manuf.* 67, 103498 <https://doi.org/10.1016/j.addma.2023.103498>.
- Chen, G., Williams, S., Ding, J., Wang, C., Suder, W., 2022. Multi-energy source (MES) configuration for bead shape control in wire-based directed energy deposition (w-DED). *J. Mater. Process. Technol.* 304 <https://doi.org/10.1016/j.jmatprotec.2022.117549>.
- Chen, I., Lee, S., 1983. Transient temperature profiles in solids heated with scanning laser. *J. Appl. Phys.* 54 <https://doi.org/10.1063/1.332111>.
- Chen, X., Wang, C., Ding, J., Bridgeman, P., Williams, S., 2022. A three-dimensional wire-feeding model for heat and metal transfer, fluid flow, and bead shape in wire plasma arc additive manufacturing. *J. Manuf. Process.* 83, 300–312. <https://doi.org/10.1016/j.jmapro.2022.09.012>.
- Cline, H.E., 1983. An analysis of the process of recrystallization of silicon thin films with either a scanning laser or strip heater. *J. Appl. Phys.* 54 <https://doi.org/10.1063/1.332291>.
- Cline, H.E., Anthony, T.R., 1977. Heat treating and melting material with a scanning laser or electron beam. *J. Appl. Phys.* 48 <https://doi.org/10.1063/1.324261>.
- Cui, C., Guo, Z., Liu, Y., Xie, Q., Wang, Z., Hu, J., Yao, Y., 2007. Characteristics of cobalt-based alloy coating on tool steel prepared by powder feeding laser cladding. *Opt. Laser Technol.* 39 <https://doi.org/10.1016/j.optlastec.2006.12.005>.
- De, J.P., Kelly, D.W., Zienkiewicz, O.C., Babuska, I., 1983. A posteriori error analysis and adaptive processes in the finite element method: Part II—adaptive mesh refinement. *Int. J. Numer. Methods Eng.* 19 <https://doi.org/10.1002/nme.1620191104>.
- Ding, J., Colegrove, P., Mehnen, J., Ganguly, S., Almeida, P.M.S., Wang, F., Williams, S., 2011. Thermo-mechanical analysis of Wire and Arc Additive Layer Manufacturing process on large multi-layer parts. *Comput. Mater. Sci.* 50 <https://doi.org/10.1016/j.commatsci.2011.06.023>.
- Gong, M., Meng, Y., Zhang, S., Zhang, Y., Zeng, X., Gao, M., 2020. Laser-arc hybrid additive manufacturing of stainless steel with beam oscillation. *Addit. Manuf.* 33 <https://doi.org/10.1016/j.addma.2020.101180>.
- Herzog, D., Seyda, V., Wycisk, E., Emmelmann, C., 2016. Additive manufacturing of metals. *Acta Mater.* 117 <https://doi.org/10.1016/j.actamat.2016.07.019>.
- Huang, H., Murakawa, H., 2016. Thermo-mechanical analysis of line heating process by an efficient and accurate multi-level mesh refining method. *Mar. Struct.* 49 <https://doi.org/10.1016/j.marstruc.2016.09.001>.
- Huang, H., Ma, N., Murakawa, H., Feng, Z., 2019. A dual-mesh method for efficient thermal stress analysis of large-scale welded structures. *Int. J. Adv. Manuf. Technol.* 103 <https://doi.org/10.1007/s00170-019-03606-4>.
- Huang, H.-C., Usmani, A.S., 1994. Finite Element Analysis for Heat Transfer, Finite Element Analysis for Heat Transfer. Springer London. <https://doi.org/10.1007/978-1-4471-2091-9>.
- Incropera, F.P., DeWitt, D.P., Bergman, T.L., Lavine, A.S., 2007. Fundamentals of Heat and Mass Transfer in Fabrics, Water.
- Joshi, A., Bangert, W., Sevik-Muraca, E.M., 2004. Adaptive finite element based tomography for fluorescence optical imaging in tissue. *Opt. Express* 12. <https://doi.org/10.1364/opex.12.005402>.
- Kim, K., Feng, S.S., 2016. Thermal mapping using infrared thermography. In: Application of Thermo-Fluidic Measurement Techniques: An Introduction. <https://doi.org/10.1016/B978-0-12-809731-1.00008-3>.
- Li, Y., Gu, D., 2014. Thermal behavior during selective laser melting of commercially pure titanium powder: Numerical simulation and experimental study. *Addit. Manuf.* 1, 99–109. <https://doi.org/10.1016/j.addma.2014.09.001>.
- Loh, L.E., Chua, C.K., Yeong, W.Y., Song, J., Mapar, M., Sing, S.L., Liu, Z.H., Zhang, D.Q., 2015. Numerical investigation and an effective modelling on the Selective Laser Melting (SLM) process with aluminium alloy 6061. *Int. J. Heat Mass Transf.* 80 <https://doi.org/10.1016/j.ijheatmasstransfer.2014.09.014>.
- Mirazimzadeh, S.E., Pazireh, S., Urbanic, J., Hedrick, B., 2022. Investigation of effects of different moving heat source scanning patterns on thermo-mechanical behavior in direct energy deposition manufacturing. *Int. J. Adv. Manuf. Technol.* 120 <https://doi.org/10.1007/s00170-022-08970-2>.
- Noor, Y.M., Tam, S.C., Lim, L.E.N., Jana, S., 1994. A review of the Nd: YAG laser marking of plastic and ceramic IC packages. *J. Mater. Process. Tech.* 42 [https://doi.org/10.1016/0924-0136\(94\)90078-7](https://doi.org/10.1016/0924-0136(94)90078-7).
- PAVELIC V., TANBAKUCHI R., UYEHARA O.A., MYERS P.S., 1969. Experimental and Computed Temperature Histories in Gas Tungsten-arc Welding of Thin Plates. *Weld. J.* 48.
- Pearson, K., 1896. *Mathematical contributions to the theory of evolution. Proceedings R. Soc.* 60.
- Rubben, K., Mohrbacher, H., Leirman, E., 1997. Advantages of using an oscillating laser beam for the production of tailored blanks, in: *Lasers in Material Processing*. <https://doi.org/10.1117/12.281143>.
- Ruppert, J., 1995. A delaunay refinement algorithm for quality 2-dimensional mesh generation. *J. Algorithms* 18. <https://doi.org/10.1006/jagm.1995.1021>.
- Shin, H.S., Boo, S.H., 2022. Welding simulation using a reduced order model for efficient residual stress evaluation. *J. Comput. Des. Eng.* 9, 1196–1213. <https://doi.org/10.1093/jcde/qwac047>.
- Tan, Z., Guo, G.W., 1994. *Thermophysical Properties of Engineering Alloys*. Metallurgical Industry Press, Beijing.
- Wang, C., Sun, Y., Chen, G., Chen, X., Ding, J., Suder, W., Diao, C., Williams, S., 2022. A simplified modelling approach for thermal behaviour analysis in hybrid plasma arc-laser additive manufacturing. *Int. J. Heat Mass Transf.* 195, 123157 <https://doi.org/10.1016/j.ijheatmasstransfer.2022.123157>.
- Xia, Y., Lei, J., Chen, H., 2022. Effects of circular oscillating laser on microstructure and mechanical property of nickel-based superalloy by laser melting deposition. *Opt. Laser Technol.* 155 <https://doi.org/10.1016/j.optlastec.2022.108361>.